Mechanistic Investigation and Optimization of Photoredox Anti-Markovnikov Hydroamination

Yangzhong Qin,^a Qilei Zhu,^a Rui Sun,^a Jacob M. Ganley,^b Robert R. Knowles^{b,*} and Daniel G. Nocera^{a,*}

^a Department of Chemistry and Chemical Biology, Harvard University, 12 Oxford Street, Cambridge, MA 02138, USA.

ABSTRACT: The reaction mechanism and the origin of the selectivity for the photocatalytic intermolecular anti-Markovnikov hydroamination of unactivated alkenes with primary amines to furnish secondary amines has been revealed by time-resolved laser kinetics measurements of the key reaction intermediates. We show that back-electron transfer (BET) between the photogenerated aminium radical cation (ARC) and reduced photocatalyst complex (Ir(II)) is nearly absent due to rapid deprotonation of the ARC, on the sub-hundred nanosecond timescale. The selectivity for primary amine alkylation is derived from the faster addition of the primary ARCs (as compared to secondary ARCs) to alkenes. The turnover of the photocatalyst occurs via the reaction between Ir(II) and a thiyl radical; the *in situ* formation of an off-cycle disulfide from thiyl radicals suppresses this turnover, diminishing the efficiency of the reaction. With these detailed mechanistic insights, the turnover of the photocatalyst has been optimized, resulting in a greater than ten-fold improvement in the quantum yield. These improvements enabled the development of a scalable flow protocol, demonstrating a potential strategy for practical applications with improved energy efficiency and cost-effectiveness.

INTRODUCTION

Light-driven photoredox catalysis has emerged as a powerful strategy to perform organic synthesis under mild conditions by taking advantage of photons to generate highly reactive intermediates that are otherwise difficult to access with traditional methods. 1-7 Photoredox reactions, however, may confront back reactions and undesired side reactions as a result of the high reactivity of the photogenerated intermediates 8-11 leading to a diminished energy efficiency. 10,11 These back reactions must be overcome to enable the sustainable adaptation of photoredox methods, which includes the use of solar light as an energy input. 12-14 Accordingly, photoredox catalysis performed under batch reaction conditions may require intense light sources (e.g. high power LED lamps) and extended reaction times (e.g. days) to achieve appreciable yields of product. 2-7 Therefore, flow setups are

usually preferred ¹⁵⁻¹⁷ to achieve high throughput for photocatalysis. As has been shown recently by our groups ^{9-11,18,19} and others, ²⁰⁻²⁴ detailed mechanistic studies provide critical insight for improving energy efficiency and the scope of photocatalysis methods. The formation of C–N bonds via intramolecular hydroamidation photocatalysis has particularly benefitted from the detection of reactive intermediates and an understanding of their chemistry. ¹¹ Recently C–N bond formation has been achieved under mild photocatalytic conditions by hydroamination reactions between alkyl amines and unactivated alkenes, ^{25,26} demonstrating an atomeconomic strategy to furnish both secondary and tertiary amine products. These photocatalytic hydroamination reactions have relied on photoexcited iridium complexes (Ir(III)) to oxidize amines, generating reduced photocatalyst complexes (Ir(III)) along with aminium radical cations (ARCs). ARCs add to the alkenes in

Scheme 1. Previously proposed mechanism for the intermolecular hydroamination of unactivated alkenes with primary or secondary amines under photoredox conditions.

$$\begin{array}{c} R^{1} \\ NH + \\ \hline \\ R^{2} \\ \hline \\ NH \\ \hline \\ R^{2} \\ \hline \\ R^{3} \\ \hline \\ R^{3} \\ \hline \\ P^{1} \\ \hline \\ PAT catalyst RS-H \\ \hline \\ Blue light \\ \hline \\ R^{2} \\ \hline \\ R^{3} \\ \hline \\ R^{4} \\ \hline \\ R^{5} \\ \hline \\ R^{5} \\ \hline \\ R^{5} \\ \hline \\ R^{7} \\ \hline \\ R^$$

an anti-Markovnikov fashion to form product radicals ²⁷ that then react with thiols through hydrogen atom transfer (HAT) to deliver the final product (Scheme 1). ²⁸ The utility of this methodology has been demonstrated for the formation of tertiary amine products from their respective secondary amines with **IrA** (**IrA** = $[Ir(III)(dF(Me)ppy)_2-(dtbbpy)]PF_6$ and dtbbpy = 4,4'-di-*tert*-butyl-2,2'-dipyridyl) as the photocatalyst (Figure 1C). ²⁵ Strikingly, when the analogous reactions are performed on primary amines with a stronger photooxidant **IrB** (**IrB** = $[Ir(III)(dF(CF_3)ppy)_2(4,4'-d(CF_3)-bpy)]PF_6$), the secondary amine products are selectively obtained with little over-reaction to produce tertiary amines (Figure 1A). ²⁶ Such photocatalyst-dependent chemoselectivity is intriguing and provides an imperative for a detailed mechanistic understanding to improve the photochemical efficiency and enable a scalable protocol for large scale synthesis.

^b Department of Chemistry, Princeton University, Princeton, NJ 08544, USA.

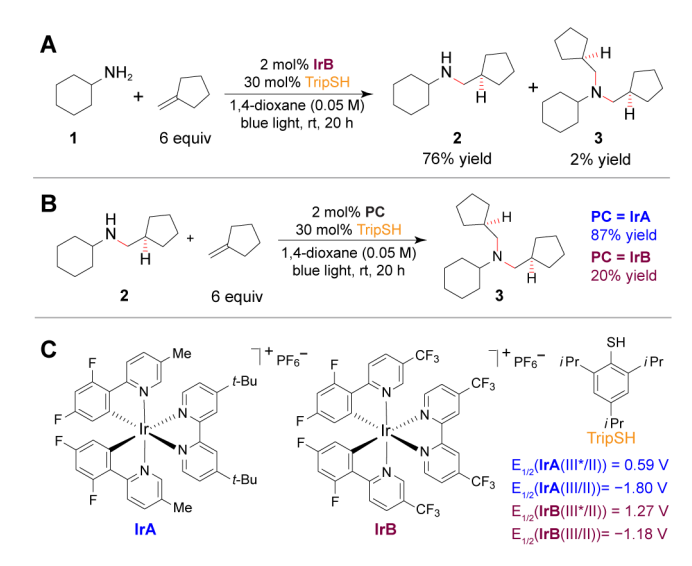


Figure 1. Product yields and selectivity achieved by different photocatalysts for the photoredox hydroamination reactions starting from (**A**) primary amine **1** and (**B**) secondary amine **2**. (**C**) Structures and redox potentials of **IrA** and **IrB** photocatalysts and HAT catalyst (TripSH). The redox potentials are referenced to Fc⁺/Fc.

Here, we present comprehensive mechanistic studies to uncover the origins of this chemoselectivity, as such insight aids in further reaction development, optimization, and application. We find that the chemoselectivity for the formation of secondary amine originates from the faster addition of the primary ARCs to the alkenes as compared to secondary ARCs. We have identified that rapid deprotonation of the ARCs, arising from their augmented acidity compared to the parent amine, is a significant nonproductive side-reaction. In addition, two critical intermediates (Ir(II) and thiyl radical) have been observed and found to be essential to the turnover of the photocatalyst, and hence, the overall reaction efficiency. With these mechanistic insights, an optimization strategy has been developed to improve the reaction efficiency, which enables relatively large-scale syntheses under scalable flow conditions for practical synthetic applications.

EXPERIMENTAL SECTION

General Considerations. All samples were prepared in a N2filled glovebox unless otherwise stated. Solvents were dried with 3 Å pre-activated molecular sieves. All commercial chemicals were purchased from Sigma Aldrich or TCI Chemicals and used as received. Photoreagents and model substrates for mechanistic studies were synthesized (Section A, SI) with their purity verified by NMR spectroscopy. For batch reactions, the solution was typically placed in a 2-dram glass vial, which was then sealed with electrical tape and illuminated with a single blue LED Kessil lamp (PR160-440nm) under constant stirring and fan-cooling (Figure S1A). The flow experiments were carried out using a custom flow setup with two Kessil lamps illuminating the reaction tubing from both sides (Figure S1B). UV-vis absorption spectra were obtained using a Cary 5000 spectrophotometer (Agilent). NMR spectra were obtained using a Bruker Avance Neo (400 M Hz) spectrometer. The product yields were determined by gas chromatography (GC, Agilent 5975C) with dibenzyl ether as the internal standard. Isolated yields were obtained for large-scale reactions (Section M, SI).

Quenching Studies. Steady-state emission spectra were measured using a QM4 fluorometer (Photon Technology International). Steady-state quenching studies were carried out using the averaged steady-state emission intensity (I) ranging from 550 nm to 600 nm, with excitation at 400 nm. Dynamic quenching studies were based on lifetimes (τ) measured by the emission decay at 600 nm with pulsed excitation at 355 nm. The Stern-Volmer quenching constant (K_{sv}) and quenching rate constant (K_{q}) were obtained using the relation: I_0/I or $\tau_0/\tau=1+K_{sv}\times$ [quencher] and $k_q=K_{sv}/\tau_0$, where I_0 and τ_0 are the emission intensity and emission lifetime, respectively, for a sample in the absence of quencher.

Electrochemical and Spectroelectrochemical Studies. All electrochemical studies were performed using a Model 760D potentiostat from CH Instruments. Cyclic voltammetry (CV) measurements were undertaken using a glassy carbon working electrode, Pt wire counter electrode, and Ag^+/Ag reference electrode, on solutions purged with N2. All CVs were referenced to the ferrocenium/ferrocene (Fc $^+/Fc$) redox couple measured under the same conditions. Spectroelectrochemical measurements were performed in a N2-filled glovebox and under similar conditions as above, except that a thin Pt mesh working electrode was placed into a 0.5 mm pathlength cuvette. The absorption spectra under an applied potential were obtained using an Ocean Optics spectrometer and Ocean View software.

Quantum Yield Measurement. The quantum yield (QY) was measured using a custom setup. Monochromic light was generated by a Kessil lamp (PR160-440nm) and a 435 nm band pass filter (FWHM = 10 nm). Passing through a lens (f = 40 mm), the light was focused onto the reaction solution (Figure 1A), which was contained in a 1-cm cuvette. The QY was determined using the following equation:

$$QY = \frac{number\ of\ product\ molecule}{number\ of\ photon\ absorbed} = \frac{cV}{\emptyset t} \tag{1}$$

where c is product concentration, V is the volume of the reaction solution, \emptyset is the photon flux and t is the reaction time. For each QY measurement, 1.2 mL of the reaction solution was used. The reaction time (t) varied from 30 min to 300 min depending on the reaction rate. The photon flux was calibrated to be 2.56×10^{-7} mol/s (corresponding to a power of 62.1 mW) based on a published procedure. ²⁹ The product concentration (c) was determined by GC with dibenzyl ether as an internal standard.

Time-Resolved Laser Spectroscopy. The laser spectroscopic setup was described in detail previously. 30 Excitation pulses at 355 nm were generated by a Quanta-Ray Nd:YAG laser (SpectraPhysics) with a repetition rate of 10 Hz and a pulse width of ~8 ns. Continuous white light, generated by a xenon-arc lamp (PTI, Model A1010), was used as the probe for the transient absorption (TA) measurements. To measure the time resolved emission decay, the excitation laser beam was focused onto the sample contained in a 1-cm path-length cuvette. The resulting emission was collected by a pair of lenses (f = 20 cm), passed through a monochromator (Triax 320) to select the wavelength, and then detected with a photomultiplier tube (PMT). To measure the TA kinetics, the sample was flowed through a 2-mm pathlength micro flow-cell (Starna Cells 583.65-Q-2/Z15) and both excitation and probe beams were focused onto the same spot on the sample. The transmitted probe beam was directed to the spectrometer and detected by the PMT. The signal of the PMT was recorded on a 1-GHz oscilloscope (LeCroy, Model 9384CM). To measure the

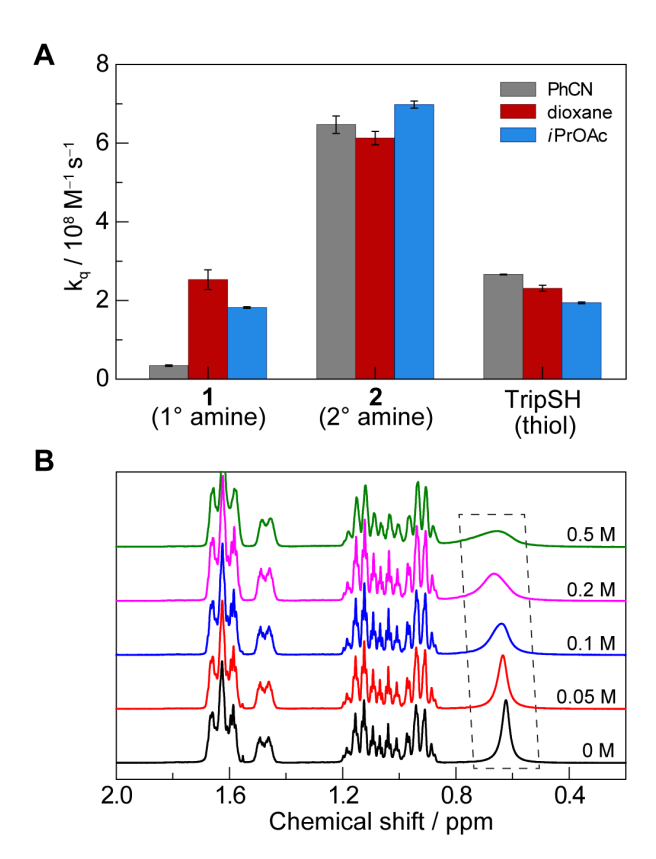


Figure 2. (**A**) Stern-Volmer quenching rate constant for the excited state ***IrB** by substrate **1**, **2** and TripSH in benzonitrile (PhCN), 1,4-dioxane, and isopropyl acetate ('PrOAc). Primary amine **1** exhibits an enhanced quenching rate in 1,4-dioxane and 'PrOAc. (**B**) ¹H NMR spectra of 20 mM substrate **1** in benzene-d₆ with various concentrations of 1,4-dioxane. The dashed gray box highlights the peak broadening and shift for the protons on the NH₂ group, indicating their H-bonding with 1,4-dioxane.

broadband TA spectra, the probe beam passing through the spectrometer was detected by a CCD camera (Andor Technology). Custom software was used for controlling the apparatus and data processing. Details of TA data analysis are provided in Section B of the SI.

RESULTS

Hydroamination Selectivity. Figure 1A shows the results for the reaction between cyclohexylamine (1) and methylenecyclopentane, with the **IrB** photocatalyst. As previously observed, ²⁶ the secondary amine (2) is the predominant product. To further confirm this chemoselectivity, the secondary amine product (2) was subjected to the same photoreaction conditions with the **IrA** and **IrB** photocatalysts (Figure 1B). We note that the oxidizing power of the photoexcited ***IrB** relative to ***IrA** ($E_{1/2}(IrB(*III/II)) = 1.27 \text{ V}$ and $E_{1/2}(*IrA(III/II)) = 0.59 \text{ V})^{26}$ is greater and thus ***IrB** should be able to photogenerate the secondary ARCs (step 1, Scheme1) with greater facility. Nevertheless, the tertiary amine 3 is obtained in only 20% yield for **IrB**, whereas a product yield of 87% is obtained for **IrA** photocatalyst (Figure 1B).

Quenching Rate and Solvent Dependence. To assess the reactivity of *IrB with primary and secondary amines (step 1, Scheme 1), Stern-Volmer quenching experiments were performed on IrB in various solvents in the presence of 1, 2 or TripSH (TripSH = 2,4,6-triisopropylbenzenethiol) (Figures 2A and S2–S4). In 1,4-

dioxane, 1 displays a quenching rate constant, kq, comparable to that of TripSH, whereas 2 displays a kq that is 2-3 times larger. In addition, quenching by TripSH showed no appreciable increase in the presence of amine (Figure S5). Surprisingly, the quenching of primary amine 1 exhibits solvent dependence whereas the secondary amine 2 and TripSH did not (Figure 2A). The 4-5-fold increase in k_q for the quenching of 1 from benzonitrile (PhCN) to 1,4-dioxane and isopropyl acetate (PrOAc) is also accompanied with a significant increase in the product yield of 2 (26% in PhCN, 76% and 79% in 1,4-dioxane and PrOAc, respectively) (Table S1, entries 1 and 2). To gain further insight into this solvent-dependent quenching behavior, ¹H NMR spectra of 20 mM 1 were measured in the presence of various concentrations of 1,4-dioxane. The broadening and shift of the NH2 peak likely suggest a H-bonding interaction between 1 and 1,4-dioxane (Figure 2B). Under similar conditions, much less broadening and peak shift were observed for diethylamine (Figure S6). Nevertheless, the quenching of the *IrB by the secondary amine is higher than by the primary amine, suggesting that the secondary amine product may inhibit the primary amine reaction upon its formation in situ. To test this inhibition effect, we performed the primary amine hydroamination reaction with and without 20 mol% 2 as shown in Table S1. A dramatically attenuated initial rate was observed after 1 h of illumination in the presence of pre-added product 2 (35% yield compared to 64% yield without secondary amine product 2, entries 5 and 6, respectively).

Back Electron Transfer, Deprotonation and Addition. The stronger quenching of *IrB by 2 than by 1 (Figure 2A) suggests that the selectivity for the primary amine (Figure 1A) cannot result from the differences in the generation of the ARCs by excited state electron-transfer (step 1, Scheme 1). We therefore turned our attention to probing the back electron transfer (BET) between the ARCs and the reduced photocatalyst, IrB(II), by examining the TA spectrum upon laser photoexcitation. Because of a weak long-lasting background signal after photoexciting IrB in 1,4-dioxane (Figure S7A), all TA spectroscopic studies were performed in PrOAc, in which *IrB decays completely to the ground state ($\tau_0 = 212 \text{ ns}$) while maintaining similar yields (Figure S7B) chemoselectivities as observed in 1,4-dioxane (Table S1, entry 2). Figure 3A shows the TA spectrum ($\lambda_{exc} = 355 \text{ nm}$) when 200 mM substrate 1 or 100 mM substrate 2 is added to a PrOAc solution of 0.2 mM IrB. The high concentration of substrate ensures that *IrB is efficiently quenched, allowing a sufficient concentration of the quenching products to be captured in the TA spectrum. The formation of IrB(II) is observed immediately after initial quenching, indicating the oxidation of the amine substrates. However, TA features of ARCs $(1^{+\bullet} \text{ or } 2^{+\bullet})$ are not detected as these species absorb in the UV region (< 300 nm), 31 which is beyond the detection range of our instrument. The spectrum of IrB(II) was confirmed independently by spectroelectrochemistry (Figure S8C). Surprisingly, IrB(II), probed at 520 nm, shows no appreciable decay up to 450 µs after the initial quenching event (Figure 3A, inset). Similarly, when *IrA was quenched by the secondary amine 2, the resulting IrA(II) signal also remained for a long time (Figures S8C and S9). These results indicate that BET between IrA(II) or IrB(II) and the primary or secondary ARCs is insignificant.

The insignificant BET may result from a fast deprotonation of the ARCs. To further verify the deprotonation pathway, we performed a photoredox deuteration reaction using the conditions shown in Figure 3B based on a published method. ³² We found 37%

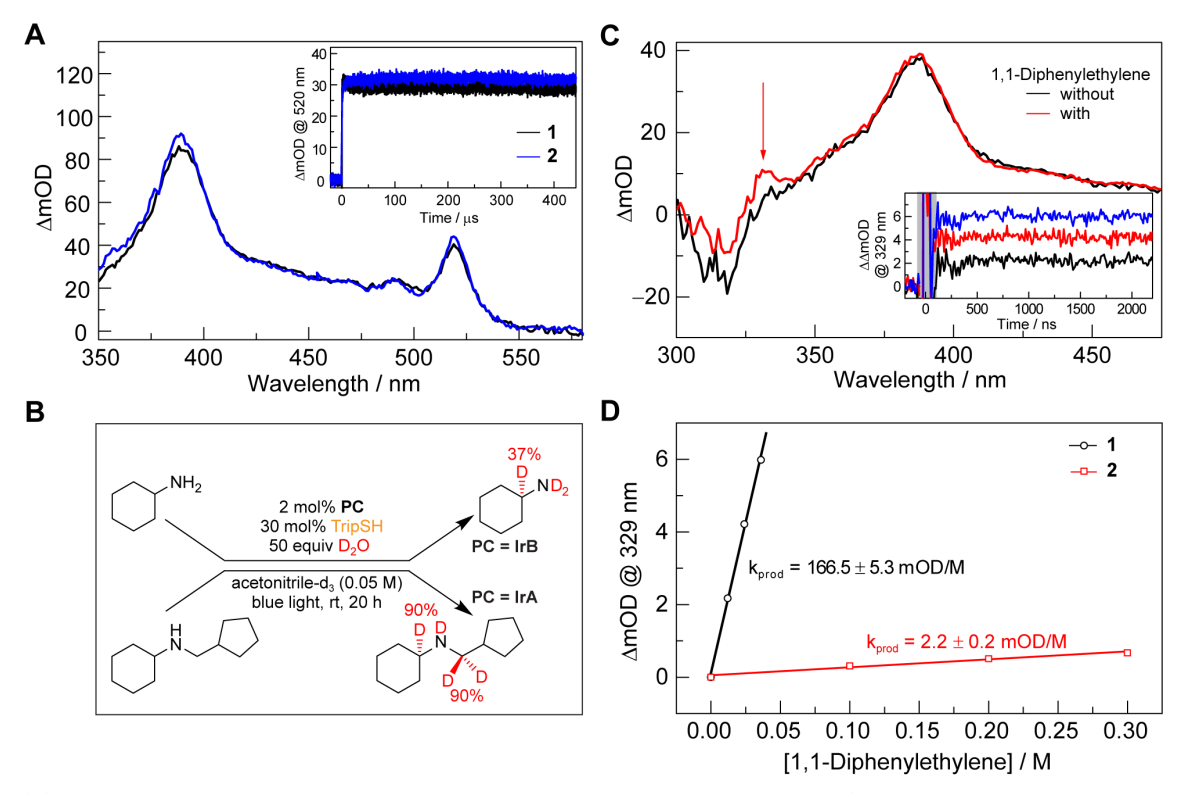


Figure 3. (A) TA spectra at 2.5 μs of a solution containing 0.2 mM IrB and 200 mM primary amine 1 (black) or 100 mM secondary amine 2 (blue). The inset shows the corresponding kinetic traces probed at 520 nm exhibiting nearly no decay, suggesting the absence of direct BET between photogenerated intermediates. (B) Deuteration reactions under photoredox conditions suggest that deprotonation can happen at the C_{α} , where the deuterated product yields are shown accordingly. (C) TA spectra at 2.5 μs of a solution containing 0.2 mM IrB and 200 mM substrate 1 in the absence (black) and presence (red) of 50 mM 1,1-diphenylethylene. The arrow highlights the TA feature centered at 329 nm, showing the intermediate after ARCs (1°+) add to 1,1-diphenylethylene. The addition kinetics (probed at 329 nm) are shown in the inset with various concentration of 1,1-diphenylethylene (12 mM (black), 24 mM (red), and 36 mM (blue)). (D) Correlations between the addition product signal and the concentration of 1,1-diphenylethylene. Different slopes (k_{prod}) suggest that 1°+ adds onto alkenes more effectively than 2°+.

deuteration on the C_α of substrate **1** and 90 % deuteration on both two C_α 's of substrate **2** based on the ¹H NMR spectra (Figure S10). In addition, based on the oxidation potential and the bond dissociation energy (BDE), we estimated the pK_a(NH) and pK_a(C_α H) of ARCs (Scheme S1 and Section K in the SI). With ethylamine as an example, pK_a(NH) and pK_a(C_α H) were calculated to be 14 and 6 in MeCN (Scheme S1A), respectively, significantly lower than the pK_a of ethylammonium (pK_a=18). For diethylamine, pK_a(NH) and pK_a(C_α H) were calculated to be 20 and 15 (Scheme S1B), respectively, in contrast to a pK_a of 19 for diethylammonium.

The addition of ARCs to alkenes (step 2, Scheme 1) was probed by TA spectroscopy using solutions containing IrB, primary amine 1, and 1,1-diphenylethylene. Figure 3C shows the TA spectra obtained at 2.5 µs for solutions containing 0.2 mM IrB and 200 mM 1 with and without 50 mM 1,1-diphenylethylene. An additional TA feature at ~330 nm was observed for the solution with 1,1diphenylethylene (Figure 3C, red) when compared to the one without (Figure 3C, black). This 330 nm feature is characteristic of the corresponding diphenyl methine radical³¹ resulting from the addition of ARC to the olefin (step 2, Scheme 1). Control experiments show that 1,1-diphenylethylene itself does not quench *IrB (Figure S11A) or contribute to the TA spectrum observed in Figure 3C (Figure S11B). To gain further kinetic information on the addition process, single-wavelength TA traces were monitored at 329 nm, where IrB(II) shows an isosbestic point with the spectrum of IrB(III) (Figure S8B). However, due to the residual signal of *IrB and potential scattering, the TA traces show a background

signal up to ~200 ns (Figure S12, black trace). To remove this background signal, the TA trace for the solution without 1,1diphenylethylene (0.2 mM IrB and 200 mM 1) was subtracted from the TA traces for similar solutions containing 1,1-diphenylethylene (Figure S12). The background-corrected TA traces are shown in the inset of Figure 3C. The product signal at 329 nm emerges at ~100 ns increases with increasing concentrations diphenylethylene (12, 24, and 36 mM). However, no clear rising feature was observed before 100 ns (Figure 3C, inset). These results suggest that the deprotonation of the ARCs occurs extremely fast on the sub-hundred nanosecond timescale. Due to the fast deprotonation, residual signal of *IrB, and scattering, we were unable to measure the addition rate constant for the ARCs. Since deprotonation can happen from both $C_{\alpha}H$ and NH groups (Scheme S1), tert-butylamine, which does not possess C_{α} -hydrogens, was also used to study the addition process. Similar results were obtained showing that the product radicals emerged at ~100 ns (Figure S13) with no clear rising features below a hundred nanoseconds. These results indicate that deprotonation occurs primarily from the NH group for primary amines.

Figure 3D (scatter plots) plots the signal of the addition product (average signal from 200 ns to 2.0 μ s at 329 nm for traces in the inset of Figure 3C) as a function of the concentration of 1,1-diphenylethylene. Linear fitting (Figure 3D, solid lines) allows for the extraction of the product radical formation rate (k_{prod}) as a function of concentrations of 1,1-diphenylethylene, which effectively reflects the addition rate of the ARCs. As shown in Figure

3D, k_{prod} was found to be ~75 times higher for primary ARCs ($1^{\bullet +}$, $k_{prod} = 166.5 \pm 5.3$ mOD/M) than for secondary ARCs ($2^{\bullet +}$, $k_{prod} = 2.2 \pm 0.2$ mOD/M). Therefore, the selectivity for primary amine (Figure 1A) correlates with a faster addition rate of the primary ARCs. Accordingly, any other photocatalyst that can oxidize primary amine should still show a selectivity similar to that of **IrB**. Indeed, this is the case. When a metal-free organic photocatalyst, **MesAcr** (**MesAcr** = 9-mesityl-3,6-di-*tert*-butyl-10-phenylacridinium tetrafluoroborate and $E_{1/2}(\text{MesAcr}^*/\text{MesAcr}^-) = 1.68 \text{ V vs}$ Fc^+/Fc), 33 was used, the primary amine reaction proceeds with similar chemoselectivity as that observed for **IrB** photocatalyst (Table S1, entries 3 and 4).

Photocatalyst Turnover Mediated by Thiyl Radical. To close a photocatalytic cycle, the reduced photocatalyst Ir(II) must return to Ir(III) (Scheme 1). To assess whether TripSH can facilitate the regeneration of the Ir(III) photocatalyst, TA studies were performed on a solution containing 0.2 mM IrB, 100 mM 2, and 30 mM TripSH (Figure 4). The TA spectrum at 200 ns in Figure 4A shows a prominent signal at 490 nm in addition to IrB(II) features at 385 nm and 520 nm. Laser excitation at 355 nm of a 15 mM Trip₂S₂ solution produces the same TA feature (Figure S14A), establishing TripS[•] as the origin of the 490 nm transient absorption. Additionally, the IrB(II) features decayed significantly for the solutions containing TripSH (Figure 4A), in contrast to the case when TripSH is absent (Figure 3A). These results implicate the reaction of TripS with IrB(II), likely with a subsequent proton transfer to reform IrB(III) and TripSH.26 Accordingly, the reaction involving thiyl radical opens another pathway to turn over the photocatalyst, which would otherwise persist as IrB(II) (Figure 3A).

The decay of the TripS^o at 490 nm occurs on a faster timescale than IrB(II) (Figure 4A). After 100 µs, TripS completely disappears whereas ~28% IrB(II) remains. The faster decay of TripS[•] is likely due to its dimerization to form disulfide Trip₂S₂. When IrB is replaced with IrA (0.2 mM IrA, 100 mM 2, and 30 mM TripSH), similar spectral profiles are observed, albeit with faster decay kinetics (Figure S15). To compare the indirect BET between TripS and the reduced photocatalyst (IrA(II) or IrB(II)), singlewavelength TA traces were probed at 520 nm (Figure 4B). Consistent with the spectral evolution, the TA traces show that **IrA(II)** decays faster than **IrB(II)**. On a longer timescale (>100 μs), the TA traces do not decay to zero (Figures 4A and S15) as a result of the prevalence of Ir(II) resulting from the formation of the disulfide. In order to quantify the kinetics of the ET reaction between Ir(II) and TripS*, TA studies were performed on a solution containing 0.2 mM IrB, 100 mM pyridine, and 30 mM TripSH (Figure S16), allowing us to determine the difference extinction coefficient ($\Delta \varepsilon$) of TripS $^{\bullet}$ (Figure S16C and Section B.1, SI). With a known $\Delta \varepsilon$ for TripS[•] and Ir(II) (Figure S8C), we extracted the ET rate constants (k_{ET}) of $2.1\pm0.1\times10^{10} \,\mathrm{M}^{-1} \,\mathrm{s}^{-1}$ and $8.1\pm0.1\times10^9 \,\mathrm{M}^{-1}$ s⁻¹ for **IrA(II)** and **IrB(II)**, respectively (Section B.2, SI).

Disulfide Formation and Accumulation of Ir(II). The formation of disulfide has a significant impact on photocatalyst turnover if it cannot be reduced by Ir(II); in this case Ir(II) will accumulate and become the resting state. This is more likely to happen for reactions with IrB due to its mild reducing potential ($E_{1/2} = -1.18\,\mathrm{V}\,\mathrm{vs}\,\mathrm{Fc}^+/\mathrm{Fc}$), which is significantly lower than the half-wave reduction potential of Trip₂S₂ ($E_{p/2} = -2.25\,\mathrm{V}\,\mathrm{vs}\,\mathrm{Fc}^+/\mathrm{Fc}$) determined by CV (Figure S17C). The TA result of residual Ir(II) in the presence of disulfide, Trip₂S₂, can be recapitulated with UV-

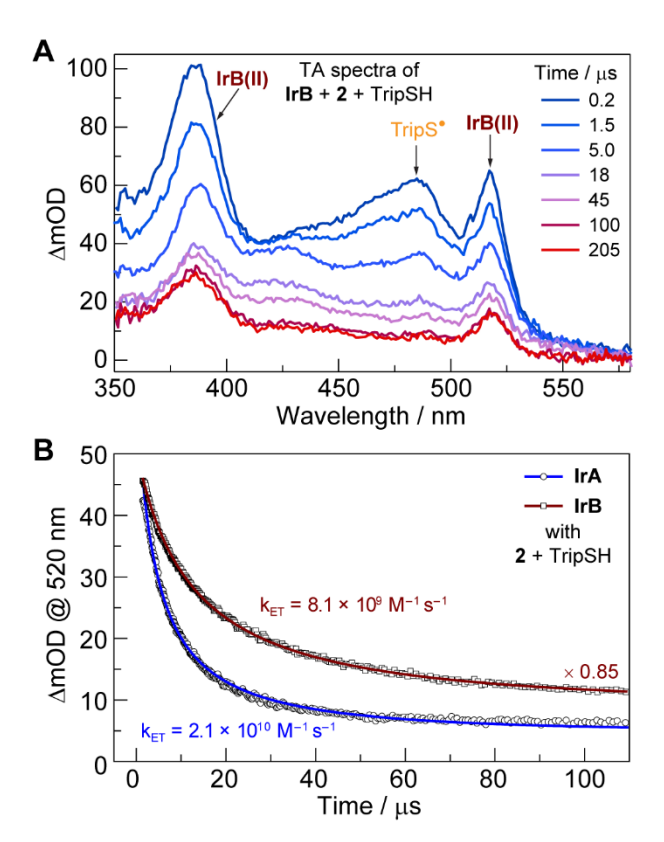


Figure 4. (**A**) TA spectra of a solution containing 0.2 mM **IrB**, 100 mM substrate **2** and 30 mM TripSH. (**B**) TA kinetics probed at 520 nm for a solution containing 100 mM substrate **2**, 30 mM TripSH, and 0.2 mM photocatalyst **IrA** or **IrB**. The faster decay for the solution with **IrA** compared to that with **IrB** indicates a faster photocatalyst turnover (see context). The scatter plots show the experimental data and the solid lines show the model fittings (Section B, SI), which allowed for the extraction of the rate constant ($k_{\rm ET}$) for the reaction between Ir(II) and TripS*.

vis spectroscopy of reacted solutions of **IrB**, which quickly turn from yellow to dark red under blue light illumination (Figure 5, inset). To quantify this color change, UV-vis absorption spectra were monitored as a function of time for the standard reaction solution (Figure 1A) contained within a screw-capped cuvette (2-mm pathlength). As shown in Figure 5, the absorption spectra evolve over 40 min to furnish a profile with maxima at 385 nm and 520 nm, which match the absorption spectrum of **IrB(II)** (Figure S8B). This dark red color of the **IrB(II)** remains stable in the sealed cuvette once generated. Subsequently exposing the solution to air causes the prompt disappearance of the dark red color as a result of the aerobic oxidation of **IrB(II)**.

To determine whether **IrB(II)** can react with Trip₂S₂, **IrB(II)** was generated photochemically (Figure 5) under standard reaction conditions (Figure 1A), after which 15 mM of Trip₂S₂ was added to the photolyzed solution. The signature absorption of **IrB(II)** at 520 nm showed nearly no change after several hours in the dark following the addition of Trip₂S₂ (Figure S18A, dark red and orange), suggesting little to no reaction between **IrB(II)** and Trip₂S₂ under the standard reaction conditions. **IrB(II)** was also generated by shining blue light on a solution containing 0.06 mM **IrB** and 50 mM **2** for 1 min (Figure S18B, dark red). Adding 15 mM Trip₂S₂ in the dark to this photolyzed solution resulted in no color change. Further illumination this solution with additional disulfide results in

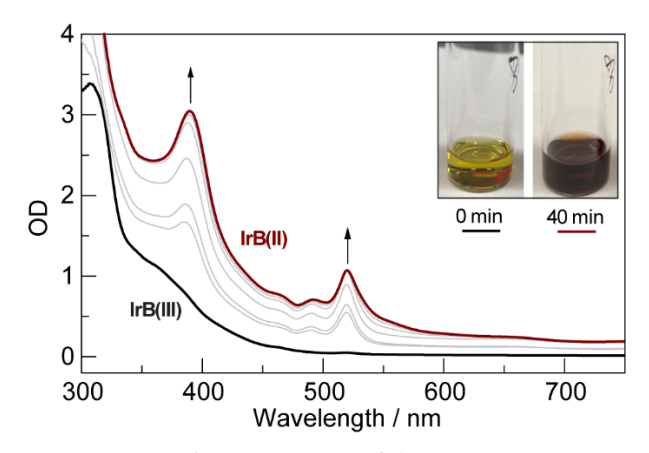


Figure 5. UV-vis absorption spectra of the primary amine reaction solution during 40-min of illumination under blue light. The reaction solution changed from an initial yellow contour to dark red, as shown by the inset, due to the accumulation of **IrB(II)**. The reaction conditions were kept identical to those shown in Figure 1A except that the solution was stored in a 2-mm path-length screw-capped cuvette for UV-vis measurements.

the disappearance of the IrB(II) (Figure S18B, pink). In contrast, when a similar experiment is performed with IrA and 2 under standard conditions (Figure 1B), IrA(II) was not observed (Figure S18C). Alternatively, IrA(II) was generated photochemically by shining blue light on a solution containing 0.1 mM IrA and 50 mM 2 for 1 min (Figure S18D, blue). Adding 15 mM Trip₂S₂ to the illuminated solution resulted in an immediate disappearance of the IrA(II) signal (Figure S18D, orange). To further confirm the reaction between IrA(II) and Trip₂S₂, IrA(II) was chemically synthesized by the treatment of IrA(III) with sodium amalgam (Section A.4, SI). The absorption spectrum of the resulting solution (Figure S19, blue) matched that of IrA(II) obtained spectroelectrochemically (Figure S8A, blue). When Trip₂S₂ was added to this IrA(II) solution, the signature absorption feature of IrA(II) at 530 nm disappeared (Figure S19, orange). Thus, Trip₂S₂ can be reduced by IrA(II) but not by IrB(II).

Reaction Optimization and Flow Chemistry. Recognizing that TripS^o dimerizes to Trip₂S₂, which **IrB(II)** is unable to reduce to regenerate the ground state IrB(III), an optimization strategy focused on increasing the concentration of TripS[•] was developed. Under the original conditions of 1 mM IrB (Figure 1A),26 the maximum possible concentration of Trip₂S₂ is 0.5 mM. Due to the limited absorption of Trip₂S₂ in the visible region (Figure S14B), this concentration does not enable TripS* to be generated substantially in the standard reaction condition (Figure 1A). Accordingly, reaction conditions were examined with the addition of excess Trip₂S₂ with the desire to increase TripS[•] upon photocleavage of the disulfide. Figure 6 summarizes quantum yields (QYs) of the secondary amine product 2 with different concentrations of thiol and/or disulfide. The QY obtained for the standard conditions of 30 mol% (15 mM) TripSH is 0.20±0.02%. Replacing 30 mol% TripSH with 30 mol% Trip₂S₂ causes a 3× increase in the QY (0.61±0.01 %), which is also higher than that obtained for 60 mol% TripSH (QY = 0.44±0.01 %). With both TripSH and Trip₂S₂ at 20 mol%, the QY further improved to 1.55±0.13%, reflecting that both TripSH and Trip₂S₂ are important to the reaction efficiency. Indeed, further boosting both the concentrations of TripSH and Trip₂S₂ to 30 mol% led to a QY of

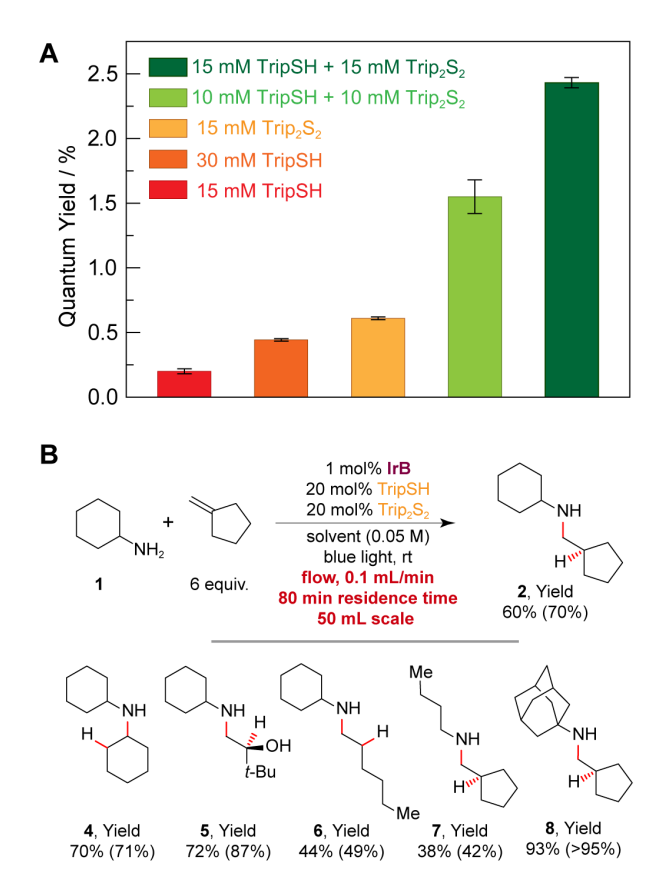


Figure 6. (**A**) Quantum yield (QY) measurements of the primary amine reaction as shown in Figure 1A. Varying the loading of TripSH and/or Trip₂S₂ results in significant increases in the QY. Standard deviations were obtained from experiments in triplicates. (**B**) Optimized reaction efficiency with additional disulfide allows for large scale (50 mL, 2.5 mmol) reactions to be performed under scalable flow conditions. A binary solvent of 1,4-dioxane and PrOAc (80:20 vol/vol) was used to solubilize **IrB**. Multiple substrates were tested on a large scale to demonstrate the general applicability of the optimized reaction strategy. Isolated yields were obtained via flash chromatography of the secondary-amine-product-derived benzamide. Yields in parentheses correspond to the secondary amines or their HCl salts, obtained from acid-base treatment of the post-illumination reaction mixture (Section M, SI).

 $2.43\pm0.04\%$, which is $12\times$ greater than the original reaction conditions (Figure 1A) for this photoredox process.

Further optimization examined the effect of the absence and presence of additional disulfide with reduced loadings of photocatalyst and alkene (Table S2). Under the standard conditions of Figure 1A, decreasing the photocatalyst loading from 2 mol% to 0.5 mol% slightly reduced the product yield from 75% to 67% (Table S2, entries 1-3). Under similar conditions with the addition of 30 mol% (15 mM) disulfide, the product yield increased from 70% to 81% with a concomitant decrease in the photocatalyst loading (Table S2, entries 4-6). The slightly lower product yield observed with additional disulfide (Table S2, entry 4) when compared to that without (Table S2, entry 1) is possibly due to over-reaction after 20 h of blue light illumination. Significantly, the yield of product is maintained with three-fold lower alkene loadings (2 equiv). Whereas a modest decrease in yield is observed for in the absence of Trip₂S₂ (Table S2, entries 1 and 8), in the presence of Trip₂S₂, the yield increases from 70% to 78% (Table S2, entries 4 and 10).

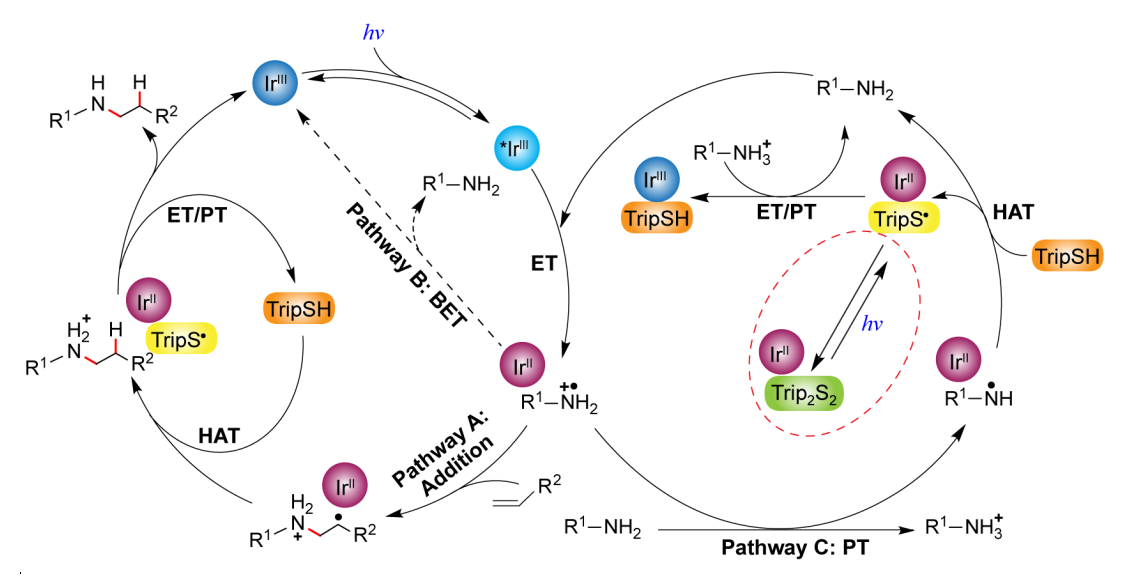


Figure 7. Complete reaction cycle for photoredox hydroamination. ET = electron transfer; BET = back electron transfer; PT = proton transfer; HAT = hydrogen atom transfer.

Interestingly, high yields hold for photocatalysts other than **IrB**. Using **MesAcr** at 4 mol% loading in the presence of Trip₂S₂ leads to appreciable product yield of the secondary amine (87%) with no detectable tertiary amine (Table S1, entry 4). These results together establish that the presence of disulfide allows the photoinduced hydroamination to be performed under reduced loadings of photocatalyst and alkene. Additionally, we also monitored the progress of the reaction with **IrB** in the presence of 30 mol% Trip₂S₂ and in the absence of TripSH. The photoreaction delivered the highest product yield of **2** (85%) in 7 h; further illumination resulted in a drop in yield of **2** from 85% to 69% with the concomitant formation of tertiary amine product **3** (Table S4).

The optimized conditions allowed the primary amine hydroamination reaction to be performed efficiently on larger scale under flow conditions. A flow reaction setup was designed comprising two Kessil lamps (440 nm) that illuminated both sides of a sample flowing through a PTFE tube (Figure S1B). The improved reaction efficiency induced by disulfide was verified for the flow setup (see Section C in the SI). For the primary amine reaction (Figure 1A) performed in the presence of 30 mol% Trip₂S₂, 60% and 73% product yields were achieved in 5 min and 10 min, respectively (Table S3). In contrast, only 11% and 14% yields were obtained after 5 and 10 min, respectively, for the photocatalysis under the original conditions (Figure 1A). Further illuminating the solution for 80 min delivered product in just 51% yield (Table S3). Large scale synthesis was demonstrated using the conditions shown in Figure 6B, top (Section C, SI), where the photocatalyst loading was halved compared to the previous reported conditions. 26 Multiple primary amine and alkene substrates were tested and showed moderate to high isolated yields (Figure 6B, bottom). All reactions were complete in 9 h on a 2.5 mmol (50 mL) scale. The flow setup may easily accommodate larger scale reactions if so desired.

DISCUSSION

A complete reaction cycle for the photoredox hydroamination reaction between primary amines and alkenes is proposed in Figure 7. The excited-state photocatalyst *Ir(III) oxidizes the amine to

generate Ir(II) and ARC with a quenching rate constant approaching the diffusion-controlled limit (Figure 2A). The generation of Ir(II) is established by the transient absorption at 385 nm and 520 nm (Figure 3A). At this juncture, the ARC may react along three possible pathways: (A) addition to alkene in a productive reaction (Figure 7, left, productive cycle); (B) direct BET with Ir(II); and (C) deprotonation to form a neutral radical (Figure 7, right, nonproductive cycle). As previously elucidated, ARC propagating along pathway A establishes the productive hydroamination.^{25,26} The addition of ARC to the alkene is conveniently examined using 1,1-diphenylethylene as its radical cation absorbs at 330 nm,³¹ which we have detected in the TA spectrum (Figure 3C). The resulting product radical cation can engage in a facile HAT reaction with TripSH (~108 M-1 s-1)34 to form the product ammonium cation and TripS, which then undergoes a reduction by Ir(II) and proton transfer to afford the desired product and regenerate both TripSH and Ir(III) (ET/PT reactions). The selectivity in this cycle originates from a difference in the kinetics between primary and secondary amines along pathway A. Pathway C enters an off-cycle reaction and is the determinant of photocatalyst turnover, which is specific to the redox properties of the Ir photocatalyst.

Origin of Chemoselectivity in the Primary Amine **Reaction**. A merit of this photoredox hydroamination method is its chemoselectivity towards the formation of secondary amine with minimal over-alkylation.²⁶ Figure 1A reproduces the selectivity for this reaction of the primary amine using IrB photocatalyst. To investigate the origin of this chemoselectivity, we examined the Stern-Volmer quenching of *IrB by the primary amine (1) and secondary amine (2). The enhanced quenching rate constant of IrB* by 2 as compared to 1 (Figure 2A) excluded the possibility that the chemoselectivity is associated with the initial quenching process (forward ET). TripSH was also observed to quench *IrB, but the quenching is insignificant considering its low concentration (15 mM) as compared to that of the amine substrate (50 mM) under the standard reaction conditions (Figure 1A). Even in the presence of amine substrate (1 or 2), the quenching by TripSH only increased slightly (Figure S5), suggesting that proton-coupled electron

transfer (PCET) does not contribute to the initial quenching to any significant extent. ^{19,35,36} The primary amine **1** shows a quenching efficiency 4-5-fold higher in 1,4-dioxane and ¹PrOAc than in PhCN, likely due to the H-bonding interaction between primary amine and 1,4-dixoane as reflected by a peak shift and broadening of the NH₂ signal in the ¹H NMR spectra shown in Figure 2B. Considering the strong and potentially deleterious competitive quenching from **2** and TripSH (Figure 2A), this increased quenching for primary amine (**1**) may play an essential role in delivering the high product yields of **2** in 1,4-dioxane (76% in Figure 1A) and ¹PrOAc (79% in Table S1, entry 2).

Pathway B may engender selectivity for the primary amine if IrB(II) reacts with 2°+ by back-electron transfer (BET) much faster than with 1°+, hence extending the lifetime of 1°+ for addition to the olefin (pathway A). However, the TA spectrum of **IrB(II)** persists over long times for both the primary and secondary amine quenching reaction (Figure 3A, inset and Figure S9), indicating that BET is not a dominant reaction pathway and moreover is not the origin of chemoselectivity. These quenching results together suggest that chemoselectivity arises from differential addition rates of the primary vs secondary ARC to alkene. Indeed, as shown in Figure 3D, the primary ARC adds to the alkene at a rate (k_{prod}) that is ~76 times greater than that for the corresponding secondary ARC. Moreover, these results suggest that the chemoselectivity for the primary amine shown in Figure 1A and Table S1 (entry 2) is inherent to the primary ARC and is not photocatalyst-specific. This contention is confirmed by the observation that chemoselectivity was maintained (Table S1, entries 3 and 4), when the primary amine reaction was performed using the organic photocatalyst MesAcr in place of IrB.

Deprotonation of ARCs. ARCs are known to undergo facile deprotonations from NH or $C_{\alpha}H$ groups to form neutral radicals, ^{27,37} as deduced primarily for secondary ARCs. ³⁸ The pK_a calculations shown in Scheme S1 suggest that deprotonation is favored from both NH and $C_{\alpha}H$ groups for primary ARCs, and only from the $C_{\alpha}H$ group for secondary ARCs, indicated by the lower pK_a values of the ARCs than their corresponding ammonium cations. To probe if deprotonation from the $C_{\alpha}H$ group does occur, ARCs were generated under photoredox conditions in the presence of D_2O and TripSH. Deprotonation from the $C_{\alpha}H$ group is supported by the results of Figures 3B and S10, which show 37% and 90% deuteration at C_{α} for primary amine 1 and secondary amine 2, respectively. These results are consistent with the pK_a calculations and confirm that deprotonation from the $C_{\alpha}H$ group indeed occurs.

TA spectroscopic studies suggest that deprotonation of the primary ARCs is faster than 100 ns. Figure 3C shows that the TA signal of the product radical cation appears promptly at 100 ns regardless of varying concentrations of 1,1-diphenylethylene (Figure 3C inset). To determine if the fast deprotonation is associated with C_αH group or the NH group, TA kinetics studies were also performed using *tert*-butylamine, which is absent of $C_{\alpha}Hs$. As shown in Figure S13, the product cation radical also appears in less than 100 ns, indicating that fast deprotonation occurs from the NH group. Based on these results, we conclude that primary ARCs predominantly deprotonate from the NH group on the sub-hundred nanosecond time scale, which is also consistent with previous reports of a short lifetime (40 ns) for primary ARCs.³⁹ The presence of fast deprotonation of the primary ARCs diverts the system to pathway C and also accounts for the absence of significant BET along pathway B in Figure 7. Additionally, the secondary ARCs are also short-lived under photoredox conditions based on similar

observations showing the absence of direct BET after the initial quenching (Figure 3A, blue plots). This is in stark contrast to the reported lifetime of a few microseconds for the secondary alkyl ARCs in acidic solution,³¹ and likely suggests that the secondary amine substrate significantly accelerates the deprotonation of ARCs under photoredox reaction conditions by acting as a base.

Pathway C diverts the system into a reaction off-cycle (Figure 7, right) because the neutral aminyl radicals formed after deprotonation are not observed to add efficiently to the alkene, as no additional rise in signal of the product radical is observed beyond 100 ns by TA spectroscopy (Figures 3C, inset and S13). This is in line with the several orders of magnitude slower addition reported for nucleophilic aminyl radicals when compared to electrophilic ARCs. 40 The carbon centered radical formed after deprotonation from the $C_{\alpha}H$ group should not react with alkene either, since the alkylation byproduct is not observed. Under the photoredox conditions shown in Figure 1A, the neutral aminyl and carbon radicals are expected to rapidly be reduced by TripSH via HAT (Figure 7, right cycle), as both reactions have been reported to proceed with rate constants of ~108 M⁻¹ s^{-1,34} Following HAT, TripS[•] and the starting materials (amines) are generated, the latter of which prevent side reactions from consuming the amine substrates.

Photocatalyst Turnover. Beyond its function as a HAT catalyst to facilitate product formation (Figure 7, left cycle) and the recovery of the amine substrate (Figure 7, right cycle), TripSH plays a critical role in mediating photocatalyst turnover.

For photoredox reactions involving IrB, TripSH provides a source of TripS^o to drive photocatalyst turnover to IrB(III). The reaction between TripS[•] and IrB(II) was studied by observing the time evolution of the TA features for IrB(II) at 385/520 nm and TripS[•] at 490 nm, respectively (Figure 4A). Moreover, the reaction between IrB(II) and TripS offers an ET/PT pathway for the photocatalyst to turnover as both IrB(II) and TripS^o decay significantly (Figure 4), in contrast to nearly no decay of IrB(II) in the absence of TripSH (Figure 3A, inset). The TripS* radical can also dimerize to form a disulfide (Trip₂S₂), resulting in an accelerated decay of TripS relative to IrB(II) decay and a residual TA signal for IrB(II) (Figure 4A). The formation the $Trip_2S_2$ will not contribute to photocatalyst turnover if IrB(II) cannot react with Trip₂S₂. Indeed, photolysis of IrB(III) in the presence of primary amine, TripSH and alkene leads to the generation of IrB(II) as monitored by UV-vis spectroscopy (Figure 5). Addition of Trip₂S₂ to this photolyzed solution of IrB(II) results in little change to the absorption profile, confirming the absence of reaction between **IrB(II)** and Trip₂S₂. However, as shown in Figure S18C, when the solution of IrB(II) and Trip₂S₂ was further subjected to illumination, IrB(II) can turnover due to the reaction between **IrB(II)** and the photogenerated thiyl radical. Therefore, for primary amine substrates, the reaction between **IrB(II)** and TripS[•] provides the only plausible path for photocatalyst turnover to IrB(III). To this end, the regeneration of TripS by Trip2S2 photocleavage22 is essential for the primary amine reaction. Figure S14 shows that Trip₂S₂ photocleavage is a facile process as the TripS[•] is formed promptly after laser excitation.

For photoredox reactions involving **IrA**, photocatalyst turnover may be driven by reaction with TripS[•] as well as by direct reaction with Trip₂S₂. Unlike the result in Figure 5 for **IrB(II)**, **IrA(II)** does not build up for the photolysis of a solution containing **IrA(III)**, secondary amine, TripSH and alkene (Figure S18C). This result

suggests superior turnover ability for **IrA** compared to **IrB**, as is observed for the faster TA decay kinetics of Ir(II) and TripS $^{\bullet}$ for **IrA** (Figure S15) as compared to **IrB** (Figure 4A). Kinetic modelling of the decay signal at 520 nm for the two photoredox reactions yields the rate constants of $k_{ET} = 2.1 \pm 0.1 \times 10^{10} \, M^{-1} \, s^{-1} \, vs \, k_{ET} = 8.1 \pm 0.1 \times 10^{9} \, M^{-1} \, s^{-1}$, respectively (Figure 4B), for the ET/PT reaction following the generation of TripS $^{\bullet}$ from TripSH by HAT. Moreover, unlike **IrB(II)**, **IrA(II)** can directly react with Trip2S2 to furnish **IrA(III)** as was verified in Figures S18D and S19, where the disappearance of **IrA(II)** was observed when Trip2S2 was added to an **IrA(II)** solution prepared either photochemically (Figure S18D) or chemically (Figure S19). Hence, in **IrA** photoredox reaction with secondary amine substrates, the regeneration of TripS $^{\bullet}$ from Trip2S2 via photolysis is not essential for photocatalyst turnover.

The differences in the turnover between IrA and IrB stem from the redox potentials of the reduced photocatalysts. Using CV (Figure S17), IrB(II) was determined to be much less reducing than IrA(II) $(E_{1/2} = -1.18 \text{ V and } -1.80 \text{ V vs Fc}^+/\text{Fc for IrB}(III/II)$ and IrA(III/II), respectively). Hence, IrA(II) can react directly with $Trip_2S_2$ and also react with $TripS^{\bullet}$ more efficiently than IrB(II) to result in photocatalyst turnover. We note that the half-peak potential for RSSR reduction (Figure S17), $E_{p/2} = -2.25 \text{ V}$ vs Fc^+/Fc , is a poor approximation of the standard potential for disulfides. In disulfides, the reduction is accompanied by irreversible bond breaking that results in a shift of E_{P/2} that is 300-600 mV more negative than the standard potential. 41 Accordingly, as shown in Figures S18B and S18D, IrA(II) is able to reduce disulfide while IrB(II) is not and **IrA**(II) is able to turnover by direct reduction of the disulfide. This additional dark reaction for IrA(II) enhances turnover and accounts for the photocatalyst dependence in the secondary amine reactions (Figure 1B), where 87% tertiary amine product 3 was obtained using **IrA**, in contrast to the 20% yield obtained using **IrB**. Moreover, as demonstrated in Table S1 (entries 5 and 6), the pre-addition of 2 decreases the primary amine reaction efficiency. This inhibition is caused by the formation of the secondary amine product due to quenching of the *IrB photocatalyst (Figure S5) thus sending the system into the off-cycle pathway (Figure 7, right).

Mechanism-Informed Reaction Optimization. The detailed mechanism reveals that the efficiency of the primary amine hydroamination reaction by IrB is compromised by photocatalyst turnover, implying that a potential optimization strategy is to increase the concentration of thiyl radicals generated via photolysis of the disulfides. As shown in Figure 6, additional disulfide results in the improvement of the quantum yield by over an order of magnitude and allows for lower loadings of photocatalyst or alkene (Table S2). We note that a HAT catalyst that cannot undergo side reactions such as dimerization may also facilitate photocatalyst turnover though TripSH remains the best HAT catalyst known to date. This is likely due to the multiple roles served by thiol and disulfide working in concert as HAT catalysts (Figure 7, left and right cycles). Though it has been shown that disulfide plays an important role in catalyst turnover in a number of radical-mediated transformations,²² thiol and disulfide together can enhance catalysis by working in concert. Whereas thiol is responsible for reducing the carbon-centered radical because of its rapid HAT dynamics (left cycle, Figure 7), the disulfide plays an essential role in turning over the photocatalyst. The benefit of thiol/disulfide cooperativity is apparent in the enhanced yield shown in Figure 6A (orange and dark green bar).

Batch reactions typically face challenges in scale-up using large reaction vessels 42 because photoexcitation is confined to absorption of incident light at the surface of the reactor. The absorbance is particularly problematic for the primary amine reaction because of the accumulation of the IrB(II) (Figure 5), which absorbs light more strongly than IrB(III) (Figure S8B) and thus manifests a strong inner filter effect as the photoredox reaction proceeds. Under flow conditions, the inner filter effect may be attenuated by irradiating the same quantity of solution in unit time as a batch reactor but over a shorter pathlength. Additionally, the quantum yield of the overall reaction of IrB with primary amine is significantly increased with the addition of Trip₂S₂. This increased quantum yield allows the photoreaction to proceed with a shortened residence time under flow conditions as demonstrated in Table S3, which lists product yields of the photoredox reaction performed in the flow reactor for given time periods of irradiation. Together, the shorted pathlength enabled by the flow reactor and the increased QY with additional Trip₂S₂ permitted a relatively large-scale synthesis to be performed with reduced loading of the photocatalyst as shown in Figure 6B.

CONCLUSION

A detailed mechanistic study of the photoredox anti-Markovnikov hydroamination of alkenes reveals that the reaction selectivity for primary amines over their secondary amine products is inherent to the addition kinetics of ARCs to the alkene. For primary amines, the rate of addition is nearly two orders of magnitude faster than that of secondary ARCs. The BET between photogenerated species (Ir(II) complexes and ARCs) is circumvented by the fast deprotonation (<100 ns) of the ARCs. Instead, a reaction between Ir(II) and thiyl radical was discovered to be essential in facilitating the photocatalyst turnover. This process is retarded by the formation of disulfide, which must be photolyzed to form thiyl radicals to turn over the photocatalyst. Finally, we optimized the photocatalyst turnover and achieved a quantum yield increase in excess of an order of magnitude compared to the previously reported conditions. This further allowed us to demonstrate efficient large-scale reactions under scalable flow conditions. We believe that the detailed mechanism and the mechanism-informed optimization strategies will benefit practical applications of photoredox hydroamination of primary amines and other reactions.

ASSOCIATED CONTENT

Supporting Information. Materials and methods, data analysis, quantum yield measurements, photoredox catalysis setups, quenching studies, TA studies, pK_a calculations, controls and optimizations, product isolation.

AUTHOR INFORMATION

Corresponding Author

Daniel G. Nocera – Department of Chemistry and Chemical Biology, Harvard University, 12 Oxford Street, Cambridge, MA 02138–2902; orcid.org/0000-0001-5055-320X; E-mail: dnocera@fas.harvard.edu.

Robert R. Knowles – Department of Chemistry, Princeton University, Princeton, New Jersey 08544; orcid.org/0000-0003-1044-4900; E-mail: rknowles@princeton.edu.

Authors

Yangzhong Qin – Department of Chemistry and Chemical Biology, Harvard University, 12 Oxford Street, Cambridge, MA 02138; orcid.org/0000-0002-2450-521X.

Qilei Zhu – Department of Chemistry and Chemical Biology, Harvard University, 12 Oxford Street, Cambridge, MA 02138; orcid.org/0000-0002-6360-9820.

Rui Sun – Department of Chemistry and Chemical Biology, Harvard University, 12 Oxford Street, Cambridge, MA 02138; orcid.org/0000-0002-3894-8425.

Jacob M. Ganley – Department of Chemistry, Princeton University, Princeton, New Jersey 08544; orcid.org/0000-0001-7705-2886.

REFERENCES

- (1) Narayanam, J. M. R.; Stephenson, C. R. J. Visible Light Photoredox Catalysis: Applications in Organic Synthesis. *Chem. Soc. Rev.* **2011**, *40*, 102–113
- (2) Shaw, M. H.; Twilton, J.; MacMillan, D. W. C. Photoredox Catalysis in Organic Chemistry. *J. Org. Chem.* **2016**, *81*, 6898–6926.
- (3) Romero, N. A.; Nicewicz, D. A. Organic Photoredox Catalysis. *Chem. Rev.* **2016**, *116*, 10075–10166.
- (4) Skubi, K. L.; Blum, T. R.; Yoon, T. P. Dual Catalysis Strategies in Photochemical Synthesis. *Chem. Rev.* **2016**, *116*, 10035–10074.
- (5) Matsui, J. K.; Lang, S. B.; Heitz, D. R.; Molander, G. A. Photoredox-Mediated Routes to Radicals: The Value of Catalytic Radical Generation in Synthetic Methods Development. *ACS Catal.* **2017**, *7*, 2563–2575.
- (6) Twilton, J.; Le, C.; Zhang, P.; Shaw, M. H.; Evans, R. W.; MacMillan, D. W. C. The Merger of Transition Metal and Photocatalysis. *Nat. Rev. Chem.* **2017**, *1*, 0052.
- (7) McAtee, R. C.; McClain, E. J.; Stephenson, C. R. J. Illuminating Photoredox Catalysis. *Tr. Chem.* **2019**, *1*, 111–125.
- (8) Shields, B. J.; Kudisch, B.; Scholes, G. D.; Doyle, A. G. Long-Lived Charge-Transfer States of Nickel(II) Aryl Halide Complexes Facilitate Bimolecular Photoinduced Electron Transfer. J. Am. Chem. Soc. 2018, 140, 3035–3039.
- (9) Sun, R.; Qin, Y.; Ruccolo, S.; Schnedermann, C.; Costentin, C.; Nocera, D. G. Elucidation of a Redox-Mediated Reaction Cycle for Nickel-Catalyzed Cross Coupling. *J. Am. Chem. Soc.* **2019**, *141*, 89–93.
- (10) Qin, Y.; Sun, R.; Gianoulis, N. P.; Nocera, D. G. Photoredox Nickel-Catalyzed C–S Cross-Coupling: Mechanism, Kinetics, and Generalization. *J. Am. Chem. Soc.* **2021**, 143, 2005–2015.
- (11) Ruccolo, S.; Qin, Y. Z.; Schnedermann, C.; Nocera, D. G. General Strategy for Improving the Quantum Efficiency of Photoredox Hydroamidation Catalysis. J. Am. Chem. Soc. 2018, 140, 14926–14937.
- (12) Schultz, D. M.; Yoon, T. P. Solar Synthesis: Prospects in Visible Light Photocatalysis. *Science* **2014**, 343, 1239176.
- (13) Qin, Y. Z.; Martindale, B. C. M.; Sun, R.; Rieth, A. J.; Nocera, D. G. Solar-Driven Tandem Photoredox Nickel-Catalysed Cross-Coupling Using Modified Carbon Nitride. *Chem. Sci.* **2020**, *11*, 7456–7461.
- (14) Crisenza, G. E. M.; Melchiorre, P. Chemistry Glows Green with Photoredox Catalysis. *Nat. Commun.* **2020**, *11*, 8–11.
- (15) Garlets, Z. J.; Nguyen, J. D.; Stephenson, C. R. J. The Development of Visible-Light Photoredox Catalysis in Flow. *Isr. J. Chem.* **2014**, *54*, 351–360
- (16) Sambiagio, C.; Noel, T. Flow Photochemistry: Shine Some Light on Those Tubes! *Tr. Chem.* **2020**, *2*, 92–106.
- (17) Corcoran, E. B.; McMullen, J. P.; Levesque, F.; Wismer, M. K.; Naber, J. R. Photon Equivalents as a Parameter for Scaling Photoredox Reactions in Flow: Translation of Photocatalytic C-N Cross-Coupling from Lab Scale to Multikilogram Scale. *Angew. Chem. Int. Ed.* **2020**, *59*, 11964–11968.
- (18) Sun, R.; Qin, Y.; Nocera, D. G. General Paradigm in Photoredox Ni-Catalyzed Cross-Coupling Allows for Light-Free Access to Reactivity. *Angew. Chem. Int. Ed.* **2020**, *59*, 2–9.

Funding Sources

This work was supported by the National Science Foundation under grant CHE-1855531 (DGN) and the National Institutes of Health under grant R35-GM134893 (RRK).

Notes

The authors declare no competing financial interest.

ACKNOWLEDGMENT

We thank Dr. Adam Rieth for helpful discussions for mechanistic insights.

- (19) Qiu, G. Q.; Knowles, R. R. Understanding Chemoselectivity in Proton-Coupled Electron Transfer: A Kinetic Study of Amide and Thiol Activation. J. Am. Chem. Soc. 2019, 141, 16574–16578.
- (20) Woodhouse, M. D.; McCusker, J. K. Mechanistic Origin of Photoredox Catalysis Involving Iron(II) Polypyridyl Chromophores. *J. Am. Chem. Soc.* **2020**, *142*, 16229–16233.
- (21) Tian, L.; Till, N. A.; Kudisch, B.; MacMillan, D. W. C.; Scholes, G. D. Transient Absorption Spectroscopy Offers Mechanistic Insights for an Iridium/Nickel-Catalyzed C-O Coupling. *J. Am. Chem. Soc.* **2020**, *142*, 4555–4559.
- (22) Romero, N. A.; Nicewicz, D. A. Mechanistic Insight into the Photoredox Catalysis of Anti-Markovnikov Alkene Hydrofunctionalization Reactions. *J. Am. Chem. Soc.* **2014**, *136*, 17024–17035.
- (23) Kim, S.; Toste, F. D. Mechanism of Photoredox-Initiated C-C and C-N Bond Formation by Arylation of IprAu(I)-CF₃ and IprAu(I)-Succinimide. *J. Am. Chem. Soc.* **2019**, *141*, 4308–4315.
- (24) Till, N. A.; Tian, L.; Dong, Z.; Scholes, G. D.; MacMillan, D. W. C. Mechanistic Analysis of Metallaphotoredox C-N Coupling: Photocatalysis Initiates and Perpetuates Ni(I)/Ni(III) Coupling Activity. *J. Am. Chem. Soc.* **2020**, *142*, 15830–15841
- (25) Musacchio, A. J.; Lainhart, B. C.; Zhang, X.; Naguib, S. G.; Sherwood, T. C.; Knowles, R. R., Catalytic Intermolecular Hydroaminations of Unactivated Olefins with Secondary Alkyl Amines. *Science* **2017**, *355*, 727–730.
- (26) Miller, D. C.; Ganley, J. M.; Musacchio, A. J.; Sherwood, T. C.; Ewing, W. R.; Knowles, R. R., Anti-Markovnikov Hydroamination of Unactivated Alkenes with Primary Alkyl Amines. *J. Am. Chem. Soc.* **2019**, *141*, 16590–16594.
- (27) Chow, Y. L.; Danen, W. C.; Nelsen, S. F.; Rosenblatt, D. H. *Chem. Rev.* **1978**, 78, 243–274.
- (28) Ganley, J. M.; Murray, P. R. D.; Knowles, R. R. Photocatalytic Generation of Aminium Radical Cations for C–N Bond Formation. *ACS Catal.* **2020**, *10*, 11712–11738.
- (29) Hatchard, C. G.; Parker, C. A. A New Sensitive Chemical Actinometer II. Potassium Ferrioxalate as a Standard Chemical Actinometer. *Proc. R. Soc. London, Ser. A* **1956**, 235, 518–536.
- (30) Holder, P. G.; Pizano, A. A.; Anderson, B. L.; Stubbe, J.; Nocera, D. G. Deciphering Radical Transport in the Large Subunit of Class I Ribonucleotide Reductase. *J. Am. Chem. Soc.* **2012**, *134*, 1172–1180.
- (31) Wagner, B. D.; Ruel, G.; Lusztyk, J. Absolute Kinetics of Aminium Radical Reactions with Olefins in Acetonitrile Solution. *J. Am. Chem. Soc.* **1996**, *118*, 13–19.
- (32) Loh, Y. Y.; Nagao, K.; Hoover, A. J.; Hesk, D.; Rivera, N. R.; Colletti, S. L.; Davies, I. W.; MacMillan, D. W. C., Photoredox-Catalyzed Deuteration and Tritiation of Pharmaceutical Compounds. *Science* **2017**, 358, 1182–1187.
- (33) Joshi-Pangu, A.; Levesque, F.; Roth, H. G.; Oliver, S. F.; Campeau, L. C.; Nicewicz, D.; DiRocco, D. A. Acridinium-Based Photocatalysts: A Sustainable Option in Photoredox Catalysis. *J. Org. Chem.* **2016**, *81*, 7244–7249.

- (34) Horner, J. H.; Martinez, F. N.; Musa, O. M.; Newcomb, M.; Shahin, H. E., Kinetics of Dialkylaminium Cation-Radical Reactions Radical Clocks, Solvent Effects, Acidity Constants, and Rate Constants for Reactions with Hydrogen-Atom Donors. *J. Am. Chem. Soc.* **1995**, *117*, 11124–11133.
- (35) Nguyen, S. T.; Zhu, Q.; Knowles, R. R. PCET-Enabled Olefin Hydroamidation Reactions with N-Alkyl Amides. *ACS Catal.* **2019**, *9*, 4502–4507.
- (36) Cukier, R. I.; Nocera, D. G. Proton-Coupled Electron Transfer. *Annu. Rev. Phys. Chem.* **1998**, 49, 337–369.
- (37) Griesbeck, A.; Oelgemöller, M.; Ghetti, F. CRC Handbook of Organic Photochemistry and Photobiology, Third Edition Two Volume Set. CRC Press: 2019
- (38) Belevsky, V. N.; Bugaenko, L. T.; Quan, O. I. Ion-Molecular Reactions of Primary Radical Cations of Aliphatic-Amines in Freon Matrices. *J. Radioanal. Nucl. Chem.* **1986**, *107*, 67–80.

- (39) Sosnovsky, D. V.; Morozova, O. B.; Yurkovskaya, A. V.; Ivanov, K. L. Relation between CINDP Formed Upon Geminate and Bulk Recombination of Radical Pairs. *J. Chem. Phys.* **2017**, *147*, 024303.
- (40) Musa, O. M.; Horner, J. H.; Shahin, H.; Newcomb, M. A Kinetic Scale for Dialkylaminyl Radical Reactions. *J. Am. Chem. Soc.* **1996**, *118*, 3862–3868.
- (41) Antonello, S.; Benassi, R.; Gavioli, G.; Taddei, F.; Maran, F. Theoretical and Electrochemical Analysis of Dissociative Electron Transfers Proceeding through Formation of Loose Radical Anion Species: Reduction of Symmetrical and Unsymmetrical Disulfides. *J. Am. Chem. Soc.* **2002**, *124*, 7529–7538.
- (42) Ravetz, B. D.; Tay, N. E. S.; Joe, C. L.; Sezen-Edmonds, M.; Schmidt, M. A.; Tan, Y.; Janey, J. M.; Eastgate, M. D.; Rovis, T. Development of a Platform for Near-Infrared Photoredox Catalysis. *ACS Cent. Sci.* **2020**, *6*, 2053–2059.

